RESEARCH ARTICLE

Key Points:
- The deglacial to Holocene upper ocean hydrography off Peru is reconstructed
- Interacting sea surface and subsurface oceanographic changes are driven by different processes
- Seasonally changing surface water masses shape thermocline depth

Correspondence to:
D. Nürnberg,
dnuernberg@geomar.de

Sea surface and subsurface circulation dynamics off equatorial Peru during the last ~17 kyr

Dirk Nürnberg[1], Tebke Böschen[1], Kristin Doering[2], Elfi Mollier-Vogel[2], Jacek Raddatz[1], and Ralph Schneider[2]

[1]GEOMAR Helmholtz Centre for Ocean Research Kiel, Kiel, Germany, [2]Institute of Geosciences, University of Kiel, Kiel, Germany

Abstract The complex deglacial to Holocene oceanographic development in the Gulf of Guayaquil (Eastern Equatorial Pacific) is reconstructed for sea surface and subsurface ocean levels from (isotope) geochemical proxies based on marine sediment cores. At sea surface, southern sourced Cold Coastal Water and tropical Equatorial Surface Water/Tropical Surface Water are intimately related. In particular since ~10 ka, independent sea surface temperature proxies capturing different seasons emphasize the growing seasonal contrast in the Gulf of Guayaquil, which is in contrast to ocean areas further offshore. Cold Coastal Water became rapidly present in the Gulf of Guayaquil during the austral winter season in line with the strengthening of the Southeast Trades, while coastal upwelling off Peru gradually intensified and expanded northward in response to a seasonally changing atmospheric circulation pattern affecting the core locations intensively since 4 ka BP. Equatorial Surface Water, instead, was displaced and Tropical Surface Water moved northward together with the Equatorial Front. At subsurface, the presence of Equatorial Under Current-sourced Equatorial Subsurface Water was continuously growing, prominently since ~10–8 ka B.P. During Heinrich Stadial 1 and large parts of the Bølling/Allerød, and similarly during short Holocene time intervals at ~5.1–4 ka B.P. and ~1.5–0.5 ka B.P., the admixture of Equatorial Subsurface Water was reduced in response to both short-term weakening of Equatorial Under Current strength from the northwest and emplacement by tropical Equatorial Surface Water, considerably warming the uppermost ocean layers.

1. Introduction

A number of studies attempted to decipher the sea surface and subsurface temperature (SST and subSST) evolution in the Eastern Equatorial Pacific (EEP), the contribution of the Equatorial Under Current (EUC), and the extension of the Peruvian coastal upwelling and oxygen minimum zone (OMZ) for different time periods [*Lea et al.*, 2000; *Loubere et al.*, 2003; *Kienast et al.*, 2006; *Koutavas et al.*, 2006; *Koutavas and Sachs*, 2008; *Pena et al.*, 2008; *Dubois et al.*, 2009, 2010; *Leduc et al.*, 2009; *Kienast et al.*, 2013]. Changes in the position of the Intertropical Convergence Zone (ITCZ) further modify hydrographic features in the EEP like the Equatorial Front (EF) and are thus important controling factors for the local hydrography off Peru [*Palacios*, 2004; *Fiedler and Talley*, 2006]. On interannual time scales, the El Niño–Southern Oscillation (ENSO) causes large variations in the chemical, physical, and biological conditions of this sensitive system [*McPhaden et al.*, 1998; *Koutavas and Joanides*, 2012; *Sadekov et al.*, 2013]. The main focus of this study is to resolve for seasonal contrasts in easternmost EEP SST and salinity (reflected in the $\delta^{18}O$ of seawater, $\delta^{18}O_{sw}$) and to relate the deglacial to Holocene sea surface modifications to the subsurface oceanographic development in order to identify the spatial and temporal variability of the upper ocean hydrography. We present high-resolution time series of sea surface and subsurface ocean properties off equatorial Peru covering the last ~17.3 kyr. The combined analysis of Mg/Ca, $\delta^{18}O$ and $\delta^{13}C$ from surface and subsurface dwelling foraminiferal species, the analysis of alkenones, and the comparison to similar published data sets from the EEP allow to decipher the past interaction between sea surface and subsurface water masses, the development of the thermocline, and the relationship to Peruvian upwelling and atmospheric circulation change. To resolve for mean-annual and seasonal contrasts in SST, we followed the approach of *Timmermann et al.* [2014] using the average and difference in temperature estimates derived from alkenones and foraminiferal Mg/Ca.

2. Study Area: The Eastern Equatorial Pacific

The surface-near hydrographic setting of the EEP [*Fiedler and Talley*, 2006; *Kessler*, 2006; *Montes et al.*, 2010] is characterized by the interplay between Equatorial Surface Water (ESW), Tropical Surface Water (TSW), and

Cold Coastal Water (CCW). South of the equator, ESW dominates with moderate to warm temperatures ranging from 20 to 25°C and low salinities between 33.8 and 34.8 (psu) (Figure 1) [*Wyrtki*, 1966; *Fiedler and Talley*, 2006]. To the north, TSW prevails being warmer than ESW at a similar salinity ($T > 25$°C, $S < 34$). TSW and ESW are separated by the Equatorial Front (EF), which is a steep thermal gradient limited to the upper ~100 m of the water column [*Pak and Zanefeld*, 1974; *Palacios*, 2004; *Rincón-Martínez et al.*, 2010] (Figure 1c). The position of the EF is controlled by seasonal migrations of the ITCZ and varies from an equatorial location during austral summer (January–March (JFM)) to ~3°N during austral winter (July–September (JAS)) [*Palacios*, 2004]. South of our study area at ~12–15°S, relatively cool ($T = 14$–18°C, S~35) CCW predominates [*Ayón et al.*, 2008] (Figure 1c), which contains a mixture of northward traveling waters and waters upwelled along the coasts of Chile and Peru.

Persistent Southeast Trade Winds (Figure 1a) result in an offshore Ekman transport along the Peruvian margin, which is supplied by seasonal coastal upwelling of cold, nutrient-rich waters from below [*Kessler*, 2006]. During austral winter (JAS), the northern position of the ITCZ causes an intensification of the Southeast Trades parallel to the Peruvian coast [*Wyrtki and Meyers*, 1976; *Strub et al.*, 1998], causing stronger upwelling of subsurface waters [*Karstensen and Ulloa*, 2008] and the decline in SSTs in the EEP [*Philander*, 1983; *Cane*, 2005]. The austral summer (JFM), instead, is characterized by a warm and stratified upper water column. The intensity of the Southeast Trades is further reduced, provoking the southeastward displacement of the equatorial warm water masses [*Kessler*, 2006; *Lea et al.*, 2006]. The upwelling intensity is then weakened, which results in warm SST anomalies along the Peruvian margin.

At subsurface level, Equatorial Subsurface Water (ESSW), Subantarctic Water (SAAW), and Subantarctic Mode Water (SAMW) interact (Figures 1c and 1d), affected by the eastward flowing EUC, the subsurface Southern Subsurface Counter Current (SSCC) extending into the Peru Chile Under Current (PCUC) [*Montes et al.*, 2010], and the Peru Chile Counter Current (PCCC) [*Strub et al.*, 1995]. Counteracting are the northward flowing cool and fresh ($T = 11.5$°C, $S = 33.8$) and nutrient-rich Peru Chile Current (PCC) [*Penven et al.*, 2005; *Karstensen and Ulloa*, 2008], and the westward flowing Southern Equatorial Current (SEC) [*Wyrtki*, 1967; *Kessler*, 2006]. The temperate and relatively saline ($T = 13$–14°C, $S = 34.9$), nutrient-rich ESSW [*Lukas*, 1986; *Silva et al.*, 2009], dominates the study area. The ESSW originates from the EUC and is transported southward in the PCUC [*Brink et al.*, 1983], which flows southward along the shelf in ~50–150 m water depth [*Penven et al.*, 2005; *Karstensen and Ulloa*, 2008]. Farther south, the PCUC even deepens to ~700 m [*Czeschel et al.*, 2011]. The EUC forms in the western equatorial Pacific close to Papua New Guinea, with approximately two thirds of its source water mass originating from South Pacific mode waters [*Rodgers et al.*, 2003; *Goodman et al.*, 2005]. The EUC is split by the Galápagos Islands; its northern deeper branch contributes to the volume of the ESSW at 100–250 m water depth [*Kessler*, 2006; *Karnauskas et al.*, 2010], and its saline and well-oxygenated waters can be traced to the coasts of Ecuador and Peru [*Toggweiler et al.*, 1991]. The shallower southern branch of the EUC [*Karnauskas et al.*, 2010] impinges the continent at ~5°S. Model results imply that only a fraction of EUC feeds the PCUC and only ~5% contribute to coastal upwelling [*Montes et al.*, 2010]. The EUC flow is strongest between January and June (austral summer and autumn) and weakest between July and November (austral winter and spring) [*Lukas*, 1986].

3. Material and Methods

3.1. Core Selection and Chronostratigraphy

Our study focuses on two piston cores retrieved from the Gulf of Guayaquil offshore the border between Ecuador and Peru close to the northern rim of today's OMZ [*Pfannkuche et al.*, 2011] (Figure 1a). Piston core M772-056-5 (03°44.99′ S, 81°07.48′ W, recovery 10.58 m; referred to as 056 in the following) was retrieved from 355 m water depth. Approximately 16 nautical miles further offshore, piston core M772-059-1 (03°57.01′ S, 81°19.23′ W, recovery 13.59 m; referred to as 059 in the following) was retrieved from 997 m water depth. The chronostratigraphy of both cores (see supporting information) is based on accelerator mass spectrometry radiocarbon dating (AMS[14]C) of planktonic foraminifers, supported by benthic stable oxygen isotope (δ^{18}O) stratigraphy from *Uvigerina peregrina* [*Mollier-Vogel et al.*, 2013] (see supporting information). In order to validate our proxy signals, we performed a surface sediment study based on 47 Multicorer samples (Figure 1a; see supporting information).
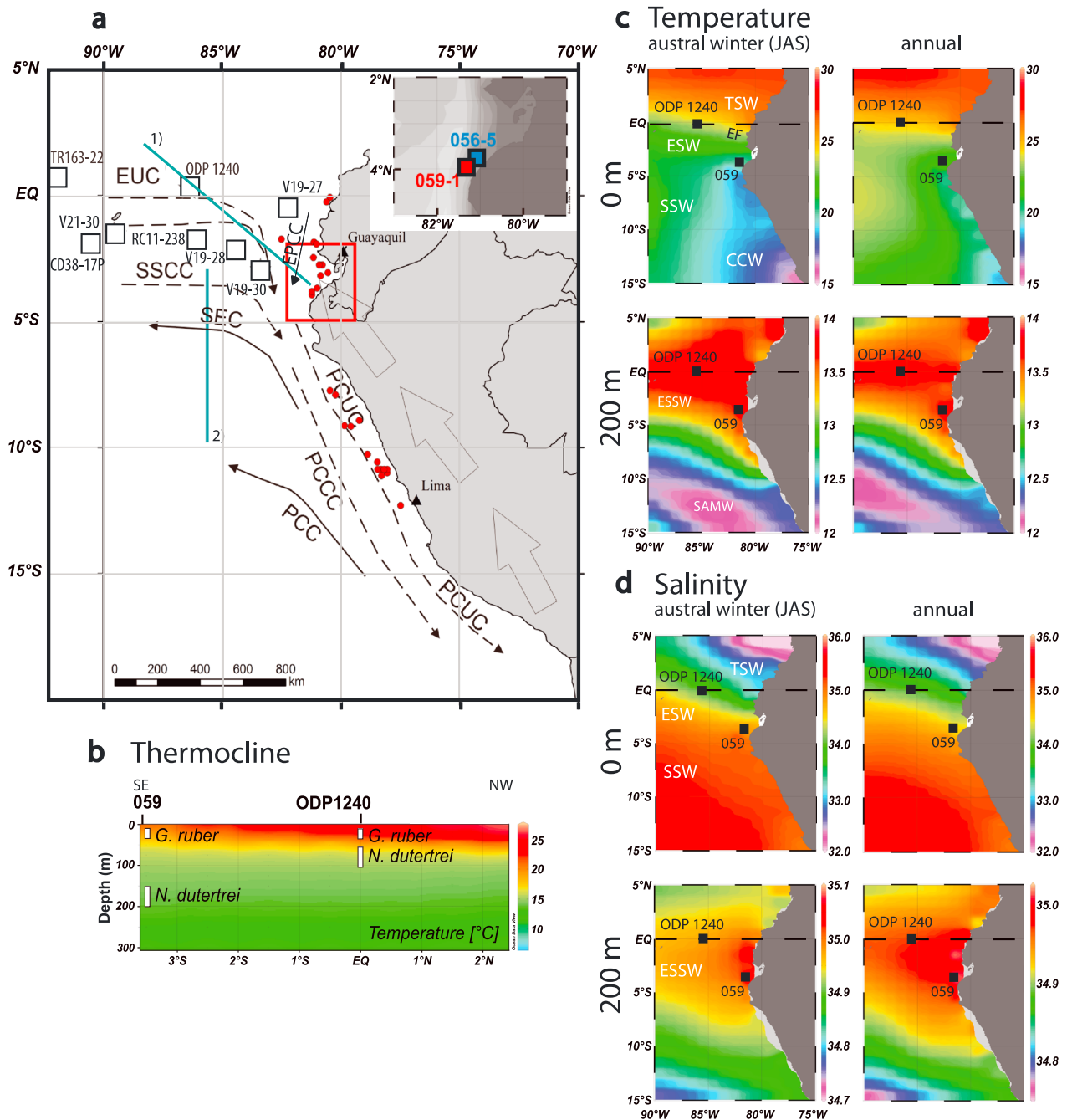
Figure 1. Study area and environmental setting. (a) Sample locations off Peru and Ecuador and major currents in the EEP. The red dots mark multicorer sediment surface samples used for proxy assessment (see supporting information). Inlet shows locations of sediment cores M772-059 (997 m water depth) and M772-056 (355 m water depth) at ~3.5°S in the Gulf of Guayaquil (red frame). Reference records discussed in the text are indicated by open squares: ODP Site 1240 [*Pena et al.*, 2008], V21-30 [*Koutavas et al.*, 2006; *Koutavas and Joanides*, 2012] and RC11-238, V19-30, V19-27, V19-28 [*Koutavas et al.*, 2006; *Koutavas and Sachs*, 2008], TR163-22 [*Lea et al.*, 2006], and CD38-17P [*Sadekov et al.*, 2013]. Surface currents (solid lines): SEC (South Equatorial Current), PCC (Peru Chile Current), EPCC (Ecuador-Peru Coastal Current). Subsurface currents (dashed lines): EUC (Equatorial Under Current), SSCC (Southern Subsurface Counter Current), PCUC (Peru Chile Under Current), and PCCC (Peru Chile Counter Current). Data source: Environmental Systems Research Institute (ESRI®). The open black arrows show main wind direction [*Kessler*, 2006]. (b) WOA09 annual temperature profile depicted in Figure 1a showing thermocline depth [*Locarnini et al.*, 2010]. Selected core locations are marked for reference. Presumed calcification depths of foraminiferal species analyzed are indicated by white squares at the respective core locations. (c) Austral winter and annual ocean temperatures and salinities in the study area at surface (0 m water depth) and subsurface (200 m water depth) level (from WOA09 monthly mean values [*Antonov et al.*, 2010; *Locarnini et al.*, 2010]. The blue line (1) is WOA09 temperature profile shown in Figure 1b [*Locarnini et al.*, 2010]. The blue line (2) is WOCE track P19C [*Rubin et al.*, 1998] from Figure S2. Plots generated with ODV [*Schlitzer*, 2010]. Prominent surface and subsurface water masses are indicated [*Wyrtki*, 1967; *Ayón et al.*, 2008]: Tropical Surface Water (TSW), Equatorial Surface Water (ESW), Cold Coastal Water (CCW), Subtropical Surface Water (SSW), Equatorial Subsurface Water (ESSW), Subantarctic Mode Water (SAMW). EF = Equatorial Front separating TSW from ESW.
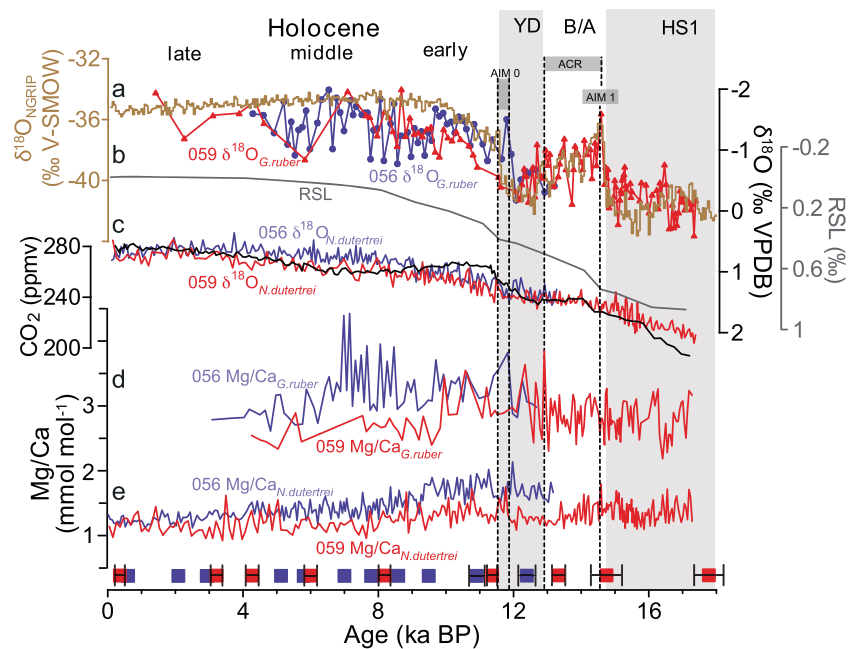
Figure 2. Planktonic foraminiferal (isotope)geochemical data from sediment cores M772-059 (red curves) and M772-056 (blue curves) in comparison to northern and southern hemisphere proxy records. (a) The $\delta^{18}O$ of *G. ruber* compared to the NGRIP (brown) climate record [*NGICP Members*, 2004]. (b) Seawater $\delta^{18}O$ ($\delta^{18}O_{sw}$) record of *Austermann et al.* [2013] reflecting global sea level change. (c) The $\delta^{18}O$ of *N. dutertrei* compared to the Antarctic (Dome Concordia) atmospheric CO_2 record (black curve [*Monnin et al.*, 2001]). (d) Mg/Ca of *G. ruber*. (e) Mg/Ca of *N. dutertrei*. Squares along *x* axis mark AMS[14]C datings for core 059 (red) and 056 (blue) [*Mollier-Vogel et al.*, 2013]. Age uncertainty (2σ) is indicated for all samples, where not visible, the uncertainty is equal or less than the symbol size (~300 years). The gray shaded areas denote the deglacial cool intervals Heinrich Stadial 1 (HS1) and Younger Dryas (YD). The stippled lines mark the Antarctic Isotope Maxima 0 (AIM 0) and 1 (AIM 1), and the Antarctic Cold Reversal (ACR).

3.2. Ocean Temperature Reconstruction and Salinity Approximation
3.2.1. Foraminiferal Stable Oxygen and Carbon Isotopes

The $\delta^{18}O$ and $\delta^{13}C$ measurements on the planktonic foraminiferal species *Neogloboquadrina dutertrei*, *Globigerinoides ruber* (white) (Figures 2a and 2c and Figure S3 in the supporting information), and on the endobenthic *Uvigerina peregrina* (Figure S1) were performed on a ThermoScientific MAT253 mass spectrometer equipped with an automated CARBO Kiel IV carbonate preparation device (GEOMAR). The isotope values were calibrated *versus* NBS 19 (National Bureau of Standards) and the in-house standard used is the "Standard Bremen" (Solnhofen limestone). Isotope values are reported in per mil (‰) relative to the VPDB (Vienna Peedee belemnite) scale. The analytical precision is $<0.06‰$ for $\delta^{18}O$ and $<0.03‰$ for $\delta^{13}C$.

3.2.2. Ocean Temperature Assessment
3.2.2.1. Foraminiferal Mg/Ca

After cleaning (see supporting information for detail), *N. dutertrei* specimens of core 059 and *G. ruber* specimens of both, surface sediment samples and cores, were analyzed with an axial-viewing ICP-OES Varian 720 at GEOMAR. Mg/Ca analyses of *N. dutertrei* of both core 056 and surface samples were carried out with the SPECTRO Ciros[CCD] SOP ICP-AES (provided with a radial plasma) at Kiel University, Germany. The ECRM 752–1 standard (3.761 mmol/mol Mg/Ca [*Greaves et al.*, 2008]) was used as an internal consistency standard to which all measurements were standardized and trend-corrected. See supporting information for further details and information on contaminants.

Mg/Ca ratios of *G. ruber* (Figure 2d) and *N. dutertrei* (Figure 2e) were converted into temperatures by using the "species specific" calibration for *G. ruber* and the "warm water" multispecies calibration, respectively, of *Regenberg et al.* [2009]. For consistency, all Mg/Ca ratios presented in this study (own data and reference data sets) were translated into temperatures using the above-mentioned calibrations. In the following, the term $SST_{Mg/Ca}$ refers to $Mg/Ca_{G.ruber}$-derived sea surface temperatures, while $subSST_{Mg/Ca}$ refers to $Mg/Ca_{N.dutertrei}$-derived subsurface temperatures.
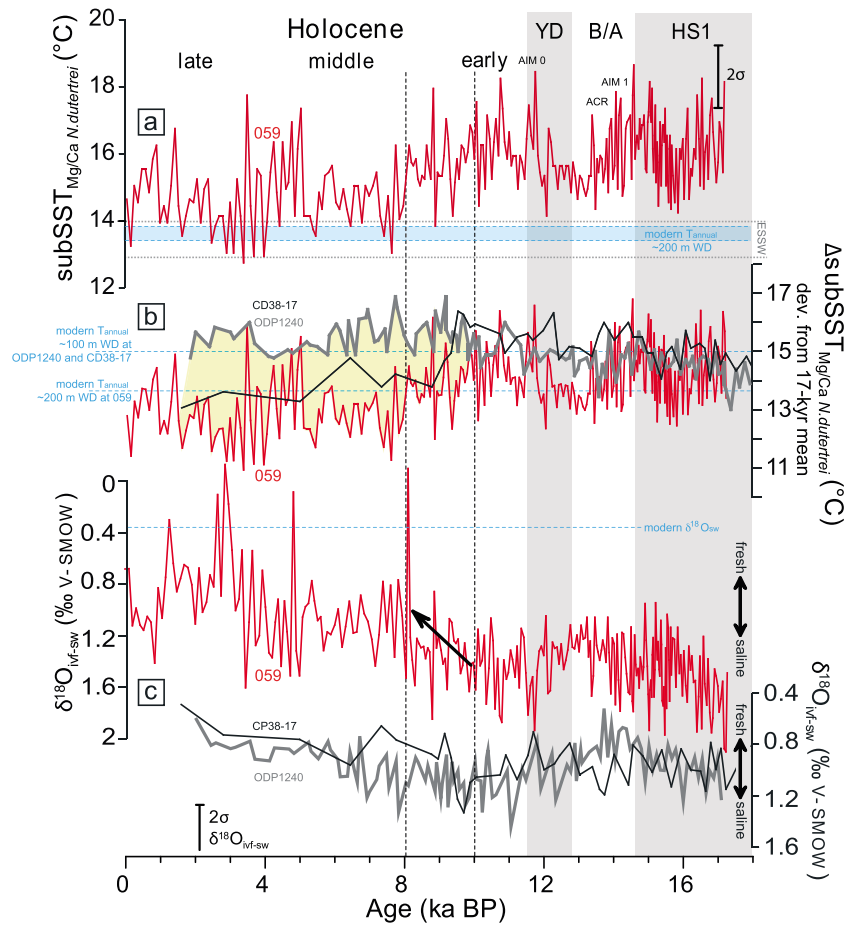
Figure 3. Ocean subsurface temperature (subSST$_{Mg/Ca}$) and salinity (assessed from ice-volume corrected δ^{18}O of seawater (δ^{18}O$_{ivf-sw}$)) development in the Gulf of Guayaquil over the last ~17 kyr in comparison to corresponding records from the EEP. (a) SubSST$_{Mg/Ca}$ derived from *N. dutertrei* (red) of core 059 (red). The blue shaded band provides the modern annual temperature at ~200 m water depth [*Locarnini et al.*, 2010]. The horizontal stippled gray lines indicate the range of subsurface temperatures of the ESSW [*Locarnini et al.*, 2010]. (b) Comparison of the 059 subSST$_{Mg/Ca}$ $_{N.dutertrei}$ record (red) to similar records from the EEP. Due to the incompatibility of foraminiferal Mg/Ca data, the subSST$_{Mg/Ca}$ $_{G.ruber}$ records are plotted as deviation from the ~17 kyr means and placed at the most reliable modern subSST estimates (horizontal hatched light blue lines) for the respective core locations [*Locarnini et al.*, 2010]: ODP Site 1240 (gray [*Pena et al.*, 2005]) and CD38-17P (black [*Sadekov et al.*, 2013]). (c) Subsurface δ^{18}O$_{ivf-sw}$ records derived from *N. dutertrei* for core 059 (this study), ODP Site 1240 (gray [*Pena et al.*, 2005]), and CD38-17P (black [*Sadekov et al.*, 2013]). The δ^{18}O$_{ivf-sw}$ records are plotted on different y axis and rather reflect relative changes in ocean salinity (see double arrow) at the respective core locations. The modern δ^{18}O$_{sw}$ value of 0.36‰ ± 0.09‰ from Station 056 averaged from 103 to 205 m water depth [*Klostermann*, 2011] is indicated by a stippled light blue line. The horizontal stippled gray lines indicate the range of subsurface δ^{18}O of the ESSW. The gray shaded areas denote the deglacial cool intervals Heinrich Stadial 1 (HS1) and Younger Dryas (YD). The vertical black stippled lines and yellowish shaded area highlight prominent changes in subSST$_{Mg/Ca}$ and subsurface δ^{18}O$_{ivf-sw}$ developments, starting particularly during 10 ka B.P. and 8 ka B.P.

The assumed habitat depth of *G. ruber* is ~30 m water depth (see supporting information). Based on a careful consideration of published data and own calculations on calcification depths of *N. dutertrei* in the study area (see supporting information), an average depth habitat of ~200 m (±~100 m) at our core locations is evident. The reconstructed late Holocene subSST$_{Mg/Ca}$ and SST$_{Mg/Ca}$ reasonably well reflect the modern conditions at the respective water depths (see supporting information; Figures 3a and 4a). For the interpretation of our SST$_{Mg/Ca}$ records derived from *G. ruber*, we acknowledge a seasonal preference of the abundance maximum toward the austral winter months during the Holocene [see *Timmermann et al.*, 2014]. SubSST$_{Mg/Ca}$ records derived from *N. dutertrei* are interpreted as annual temperature estimates (see supporting information). The important issue of calcite dissolution lowering foraminiferal Mg/Ca and hence temperature estimates is discussed in the supporting information.
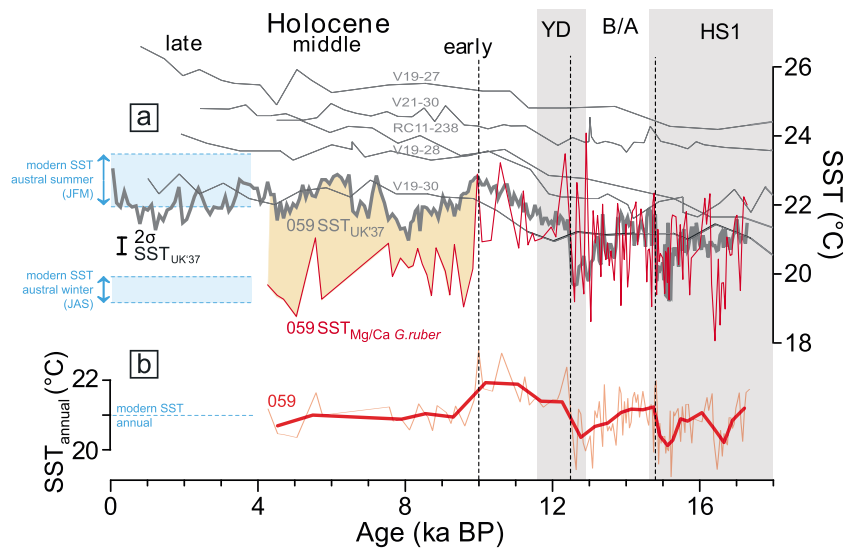
Figure 4. Ocean surface temperature (foraminiferal $SST_{Mg/Ca}$ and alkenone-based $SST_{UK'37}$) development in the Gulf of Guayaquil over the last ~17.3 kyr. (a) The $SST_{Mg/Ca}$ derived from *G. ruber* (red) of core 059 in comparison to the $SST_{UK'37}$ record of the same core (gray). The blue shaded bands provide modern austral summer (JFM) SST and modern austral winter (JAS) SST, respectively [*Locarnini et al.*, 2010]. The $SST_{UK'37}$ records of EEP cores V19-30, V19-28, RC11-238, V21-30, and V19-27 (gray) to the north, northwest, and west of our study area [*Koutavas et al.*, 2006; *Koutavas and Sachs*, 2008; *Koutavas and Joanides*, 2012] are shown for comparison (age model of core V19-30 adopted from *Kienast et al.* [2013]). (b) Estimate of annual SST (SSTannual) of core 059 averaged from the seasonally skewed alkenone and foraminiferal SST proxies ((SSTMg/Ca + SSTUK'37)/2). The gray shaded areas denote the deglacial cool intervals Heinrich Stadial 1 (HS1) and Younger Dryas (YD). The vertical black stippled lines and orange shaded area highlight prominent changes in $SST_{Mg/Ca}$ and $SST_{UK'37}$ developments.

3.2.2.2. Alkenone Temperatures

In addition to Mg/Ca-derived ocean temperatures, sea surface temperatures were derived from the alkenone unsaturation index ($U^{K'}_{37}$) (Figure 4a). Details on methods and calibration of alkenones are provided in the supporting information. According to our considerations, today $SST_{UK'37}$ most likely records the austral summer season in our working area. Such notion is supported by studies in the Peruvian upwelling [*Prahl et al.*, 2010] and in the Gulf of California [*Goñi et al.*, 2001], showing that at low latitudes the $SST_{UK'37}$ signal is skewed seasonally toward the summer season, when surface waters are warmest and the coccolithophorid and, thus alkenone flux, is highest.

3.2.3. Salinity Approximated From the Oxygen Isotope Signature of Seawater

Regional variations of subsurface and sea surface salinity were approximated from $\delta^{18}O_{sw}$ [e.g., *Nürnberg*, 2000; *Nürnberg et al.*, 2008] (Figures 3c and 5b), which was calculated by combining the Mg/Ca-derived temperatures (Figures 3a and 4a) and the corresponding $\delta^{18}O$ values of the same foraminiferal species (Figures 2d and 2e). First, the temperature effect was removed from the initial foraminiferal $\delta^{18}O$ by using the temperature versus $\delta^{18}O_{calcite}$ equation of *Thunell et al.* [1999] resolved toward $\delta^{18}O_{sw}$. Second, we generated the regional ice volume free $\delta^{18}O_{sw}$ record ($\delta^{18}O_{ivf-sw}$) by accounting for changes in global $\delta^{18}O_{sw}$ due to continental ice volume variability using the relative Barbados sea level curve of *Austermann et al.* [2013] (Figure 2b). The error in $\delta^{18}O_{ivf-sw}$ is assumed to be close to ~±0.4 ‰, based on the approach in error propagation analysis by *Bahr et al.* [2013]. We are aware that downcore $\delta^{18}O_{ivf-sw}$ variations are rather small although reliable, as they match other independent proxy parameters. We refrain from converting the $\delta^{18}O_{ivf-sw}$ values into salinities, as it is not warranted that the modern linear relationship between $\delta^{18}O_{sw}$ and salinity holds through time.

4. Results and Discussion

4.1. Subsurface Water Mass Property Changes Over the Last ~17 kyr

The subSST$_{Mg/Ca}$ of core 059, which are considered to reflect annual conditions (see supporting information), scatter between ~15 and 18°C during deglacial times and the early Holocene (Figure 3a), intercalated by
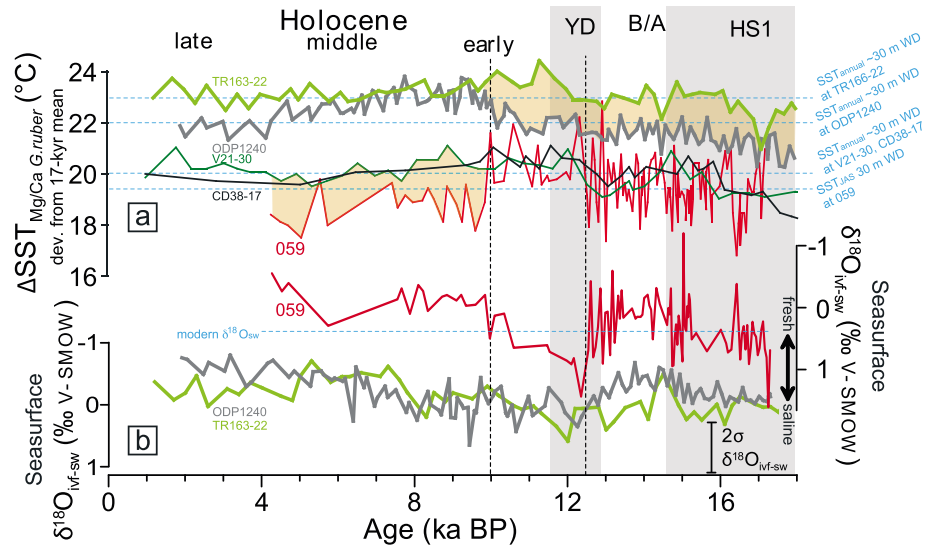
Figure 5. Ocean surface temperature (SST$_{Mg/Ca}$) and salinity (assessed from ice-volume corrected δ^{18}O of seawater (δ^{18}O$_{ivf-sw}$)) development in the Gulf of Guayaquil over the last ~17.3 kyr in comparison to records from the EEP. (a) Comparison of the core 059 SST$_{Mg/Ca\ G.ruber}$ record (red) to similar records from the EEP. Due to the incompatibility of foraminiferal Mg/Ca data, the SST$_{Mg/Ca\ G.ruber}$ records are plotted as deviations from the ~17.3 kyr means and placed at the most reliable modern SST estimates (horizontal hatched light blue lines) for the respective core locations [*Locarnini et al.*, 2010]: TR163-22 (light green [*Lea et al.*, 2006]), ODP Site 1240 (gray [*Pena et al.*, 2005]), V21-30 (green [*Koutavas and Joanidis*, 2012]), and CD38-17P (black [*Sadekov et al.*, 2013]). (b) Surface δ^{18}O$_{ivf-sw}$ records derived from *G. ruber* for core 059 (this study), ODP Site 1240 (gray [*Pena et al.*, 2005]), and TR163-22 (light green [*Lea et al.*, 2006]). Due to the incompatibility of foraminiferal Mg/Ca data, the δ^{18}O$_{ivf-sw}$ records are plotted on different y-axes and rather reflect relative changes in ocean salinity (see double arrow) at the respective core locations. The modern δ^{18}O$_{sw}$ value of 0.33 ± 0.11‰ from the Gulf of Guayaquil (Station 056, averaged from 9 to 35 m water depth [*Klostermann*, 2011]) is indicated by a stippled light blue line. The gray shaded areas denote the deglacial cool intervals Heinrich Stadial 1 (HS1) and Younger Dryas (YD). The vertical black stippled lines and orange shaded areas highlight prominent changes in SST and surface δ^{18}O$_{ivf-sw}$ developments.

prominent subSST$_{Mg/Ca}$ declines during the cold Heinrich Stadial 1 (HS1: 18–14.6 ka B.P. [*Barker et al.*, 2010]) and the Antarctic Cold Reversal (ACR: 14.5–12.9 ka B.P. [*WAIS Divide Project Members*, 2013]. Notably, distinct subsurface warming of ~2°C appears during the Antarctic Isotope Maxima 1 and 0 (AIM 1: ~14.5 ka B.P.; AIM 0: 11.95–11.6 ka B.P. [*WAIS Divide Project Members*, 2013]). This deglacial pattern in subSST$_{Mg/Ca}$ is hardly reflected in the isotopic subsurface δ^{18}O$_{N.dutertrei}$ record (Figure 2c). The δ^{18}O$_{N.dutertrei}$ record gradually declines to negative values across the deglaciation and is similar to the Ocean Drilling Program (ODP) Site 1240 δ^{18}O$_{N.dutertrei}$ record (0°01.31′N, 86°27.76′W; 2,921 m water depth; located in the EEP north of the equator [*Pena et al.*, 2005, 2008]) with an overall amplitude of ~1.5‰ (see supporting information). The shape of the δ^{18}O$_{N.dutertrei}$ and δ^{18}O$_{U.peregrina}$ records resembles the Antarctic (Dome Concordia) atmospheric CO$_2$ record [*Monnin et al.*, 2001] (Figure 2c) rather than both the Antarctic [*European Project for Ice Coring in Antarctica Community Members*, 2006] and Greenland δ^{18}O climate records [*North Greenland Ice Core Project (NGICP) Members*, 2004] (see Figures S1c and S1d).

The subSST$_{Mg/Ca}$ of core 059 decline gradually by ~2°C starting at ~10 ka B.P. and reaching minimum values at ~8 ka B.P., retaining the large deglacial amplitude variations of ~2.5°C even during short periods in the Holocene (Figure 3a). The subSST$_{Mg/Ca}$ record of adjacent core 056 shows warmer and relatively constant temperatures of ~18°C during the Younger Dryas (YD) and the Early Holocene (maximum 19°C) and experiences a pronounced temperature drop of ~2°C at ~9.5 ka B.P. (compare to Figure 2e). During the middle and late Holocene, subSST$_{Mg/Ca}$ in this core continues to drop and reach ~15°C in the youngest core sections. Overall, the Holocene magnitude of subsurface cooling amounts to on average ~4°C and ~2°C in cores 056 and 059, respectively. Core 056, located closer to the coast, thus experiences a more pronounced decline in subSST$_{Mg/Ca}$ during the Holocene with the temperatures approaching those of the core 059 not before ~2–3 ka B.P. (Figure 2e). These youngest subSST$_{Mg/Ca}$ estimates are close to the modern annual temperature at ~150–200 m water depth [*Locarnini et al.*, 2010] (Figure 3a).

The cooling at subsurface depths since ~10 ka B.P. is accompanied by freshening. Subsurface $\delta^{18}O_{ivf-sw}$ values in core 059 scatter around ~1.3 ± 0.4‰ (2σ) during the deglaciation coming gradually closer to the modern $\delta^{18}O_{sw}$ value of ~0.4‰ during the middle and late Holocene [*Klostermann*, 2011] (Figure 3c). The subsurface $\delta^{18}O_{ivf-sw}$ values in core 056 are stable (~1.7 ± 0.4‰) until ~9.5 ka B.P., but lighter than in core 059 (not shown). Subsequently, a continuous freshening begins with $\delta^{18}O_{ivf-sw}$ values approaching those of core 059 during the late Holocene.

We basically assess our subSST$_{Mg/Ca}$ and subsurface $\delta^{18}O_{ivf-sw}$ reconstructions reliable, although the direct comparison to published foraminiferal Mg/Ca-data sets poses problems due to inconsistencies in the use of calibrations, foraminiferal cleaning techniques, and analytical approaches (see supporting information). When comparing to other data sets, we present the relative temporal variations in subSST$_{Mg/Ca}$ as deviation from the ~17 kyr averages (Figure 3b). The core 059 subSST$_{Mg/Ca}$ record exhibits a convincing resemblance during HS1 to core CD38-17 (1°36.04′S, 90°25.32′W; 2580 m water depth; located ~20° longitude further to the west in the EEP southwest of the Galapagos Island [*Sadekov et al.*, 2013]), and to ODP Site 1240 (Figure 1a). Afterward, the subSST$_{Mg/Ca}$ records develop differently in the different regions. The subsurface $\delta^{18}O_{ivf-sw}$ record, instead, corresponds in shape and amplitude to the according data sets of core CD38-17 and ODP Site 1240 over broadly the entire deglacial to Holocene time period (Figure 3c).

The deglacial to Holocene change from warm and saline to cool and fresh conditions at subsurface level in the Gulf of Guayaquil approaching the modern annual subSST and subSSS conditions at ~150–200 m water depth and basically supported by the same development at core CD38-17 of *Sadekov et al.* [2013] implies significant changes in the local water masses (Figure 3). Today, the prevailing subsurface water mass at the core locations is the ESSW feeding from the eastward flowing EUC and mainly transported poleward by the PCUC [*Tsuchiya and Talley*, 1998; *Chaigneau et al.*, 2013] (Figures 1c and 1d). These water masses impinge the South American coastline between 2°N and 2°S at depths between 30 and 300 m [*Lukas*, 1986]. Acoustic Doppler Current profiles in the EEP, indeed, indicate that most subsurface currents in the study area originate from a northwesterly direction [*Chaigneau et al.*, 2013]. The gradual eastward propagation and emplacement of ESSW in the Gulf of Guayaquil hold for most of the Holocene, with the exception of short time intervals during which ESSW is displaced by warm tropical waters (Figures 1c and 1d; see section 4.4).

Prior to ~10–8 ka B.P., the warmer and more saline subsurface conditions in the Gulf of Guayaquil point to the reduced admixture of ESSW most likely in response to both the weakened EUC flow and the emplacement by warm tropical waters, i.e., ESW. Important to note is that the significant subsurface change at ~10–8 ka B.P. in the Gulf of Guayaquil (core 059) and south of Galapagos (core CD38-17) is accompanied by a relative warming at ODP Site 1240 (Figure 3b). The prominent oceanographic change is independently supported by the corresponding $\delta^{13}C_{N.dutertrei}$ records. While the core 059 $\delta^{13}C_{N.dutertrei}$ record is overall lighter than the ODP Site 1240 $\delta^{13}C_{N.dutertrei}$ record, both data series merge since ~10–8 ka B.P. and remain similar until ~6 ka B.P. (see Figure S3c).

4.2. Deglacial to Holocene Changes in the EEP Uppermost Mixed Layer

The SST$_{Mg/Ca}$ record of core 059 scatters around ~21°C during the deglaciation (Figures 2d and 4a), with rather high values at the end of the last glacial period. During the Early Holocene at ~10 ka B.P., SST$_{Mg/Ca}$ in core 059 experiences a rapid cooling by ~2°C on average, which took place within a few centuries. Afterward, the SST$_{Mg/Ca}$ remained at ~20 ± 1°C for the remaining Holocene. In principal, we interpret the temporal SST$_{Mg/Ca}$ changes in terms of changing water masses, rather than in terms of direct longwave or shortwave forcing at the surface (orbital insolation or atmospheric CO_2 changes). The latter may outweigh the advective contributions from different water masses. We are indeed not able to disentangle the various contributions, but question that in particular the rapid and significant SST$_{Mg/Ca}$ drop at 10 ka B.P. might have been caused by other processes than water mass dynamics and gradual movements of steep SST fronts.

The SST$_{Mg/Ca}$ record at core location 056 exhibits on average higher temperatures by ~1°C compared to the core 059 (cf. Figure 2d). Relatively constant temperatures of ~22.5°C remain during the early Holocene and scatter between ~21.5°C and ~22.5°C at the transition between early and middle Holocene. Delayed by ~3 kyr compared to core 059, SST$_{Mg/Ca}$ of core 056 drops to ~20.5°C on average at ~8.5 ka B.P. and remains

at this temperature level (cf. Figure 2d). The SST$_{Mg/Ca}$ records of both cores end at ~4 ka B.P. due to the absence of *G. ruber* in the uppermost core section. The absolute SST$_{Mg/Ca}$ offset between cores in fact reflects the complex oceanographic setting in the Gulf of Guayaquil, where today a steep latitudinal gradient in SST develops in response to both the interaction of the CCW, ESW, and TSW and seasonal migrations of the EF [e.g., *Palacios*, 2004] (Figure 1c). Our finding of relatively warm early to middle Holocene SST$_{Mg/Ca}$ at core 056 is congruent to geoarcheological [*Andrus et al.*, 2002], paleontological [*Sandweiss et al.*, 1996], ice core [*Thompson et al.*, 1995], and modeling studies [*Liu et al.*, 2000] showing that along the coasts of northern Peru temperatures were higher by ~3–4°C compared to today until ~5 ka B.P., due to the invasion of warm, tropical water masses as far south as 10°S.

The alkenone-based SST$_{UK'37}$ record of core 059 varies between 19.5°C and 22°C during the deglaciation, with lowest temperatures during the glacial and the YD (Figure 4a). Abrupt warmings of ~2°C are seen at the beginning of the warm Bølling/Allerød (~14.8 ka B.P.) and during the YD (~12.5 ka B.P.). During the Holocene, the SST$_{UK'37}$ record varies around 22.5°C and rises to ~23°C in the core top sample. It is almost similar to the SST$_{UK'37}$ record of core V19-30 from further offshore [*Koutavas and Sachs*, 2008; *Kienast et al.*, 2013] (Figures 1a and 4a). Other SST$_{UK'37}$ records from farther to the north and northwest (V19-28, V21-30, V19-27, and RC11-238 [*Koutavas and Sachs*, 2008]) retrace the gradual deglacial to Holocene SST$_{UK'37}$ increase at core 059, although being warmer by several degrees (Figure 4a). Apparently, the area experienced broadly the same relative deglacial to Holocene thermal development at the ocean surface— at least during the season with the highest coccolithophorid production [*Leduc et al.*, 2010; *Schneider et al.*, 2010].

The core 059 δ^{18}O$_{ivf-sw}$ record based on *G. ruber* shows accentuated changes in the Gulf of Guayaquil (Figure 5b). In comparison to the subsurface δ^{18}O$_{ivf-sw}$ of *N. dutertrei* (Figure 3c), the values are on average lighter by ~0.6‰ pointing to generally fresher conditions at the sea surface. Prior to 10 ka B.P., core 059 shows high-amplitude sea surface δ^{18}O$_{ivf-sw}$ variations ranging from on average 0.8 to 0‰ and a typical deglacial northern hemisphere pattern: more saline conditions during HS1 and YD relative to the Bølling-Allerød (B/A). During the Holocene, the δ^{18}O$_{ivf-sw}$ record suggests salinity conditions comparable with the B/A conditions. The relatively stable δ^{18}O$_{ivf-sw}$ data at our core location scatter around the modern δ^{18}O$_{sw}$ value of ~0.3‰ [*Klostermann*, 2011] and come along with gradual cooling until ~4 ka B.P. (Figure 4a). At ODP Site 1240 and core TR163-22 farther to the northwest, the sea surface δ^{18}O$_{ivf-sw}$ development (recalculated from *G. ruber* δ^{18}O and Mg/Ca raw data of *Pena et al.* [2008] and *Lea et al.* [2006]) is less variable than at core 059 although relative more saline conditions during HS1 and YD prevail in all cores and relative freshening during the B/A and the Holocene (Figure 5b).

It is nearby to speculate that the SSS development in the narrow and sheltered Gulf of Guayaquil might have been affected by fluvial freshwater discharge and hence by precipitation change in the Guayas River's catchment area (see Figure 1), similarly as it was noted in δ^{18}O$_{ivf-sw}$ derived from *G. ruber* off the Mississippi delta [*Nürnberg et al.*, 2015]. As an approximation for Guayas River paleo-runoff, *Mollier-Vogel et al.* [2013] use the log(Ti/Ca) record of our core 059 revealing reduced riverine discharge during the early and middle Holocene and enhanced discharge during the deglaciation and the late Holocene. The mismatch to the sea surface δ^{18}O$_{ivf-sw}$ record might be explained by the preference of both proxies toward different seasons: the SSS approximation (δ^{18}O$_{ivf-sw}$) reflects the austral winter signal (JAS). Instead, log(Ti/Ca) most likely provides the austral summer (JFM) situation as the present-day Guayas River discharge is most prominent during austral winter, when the ITCZ over South America and in the easternmost EEP prevails south of the equator and rainfall is at maximum in the Guayas catchment area [*Rincón-Martínez et al.*, 2010; *Mollier-Vogel et al.*, 2013]. Even during the deglaciation, when the seasonal contrast was less pronounced (Figure 6a), we neither find a convincing correlation nor anticorrelation between both proxies, implying that the *G. ruber* δ^{18}O$_{ivf-sw}$ is driven by oceanic processes.

4.3. Seasonal Contrasts in the Gulf of Guayaquil

Taking into account that today in the EEP SST$_{UK'37}$ and SST$_{Mg/Ca}$ most likely provide the austral summer and winter temperatures, respectively (see section 3), the difference between both provides the seasonal contrast. The notion on seasonally skewed SST proxies [see *Timmermann et al.*, 2014] is corroborated by the fact that the late Holocene SST$_{UK'37}$ resembles the modern austral summer (JFM) SST, while the late
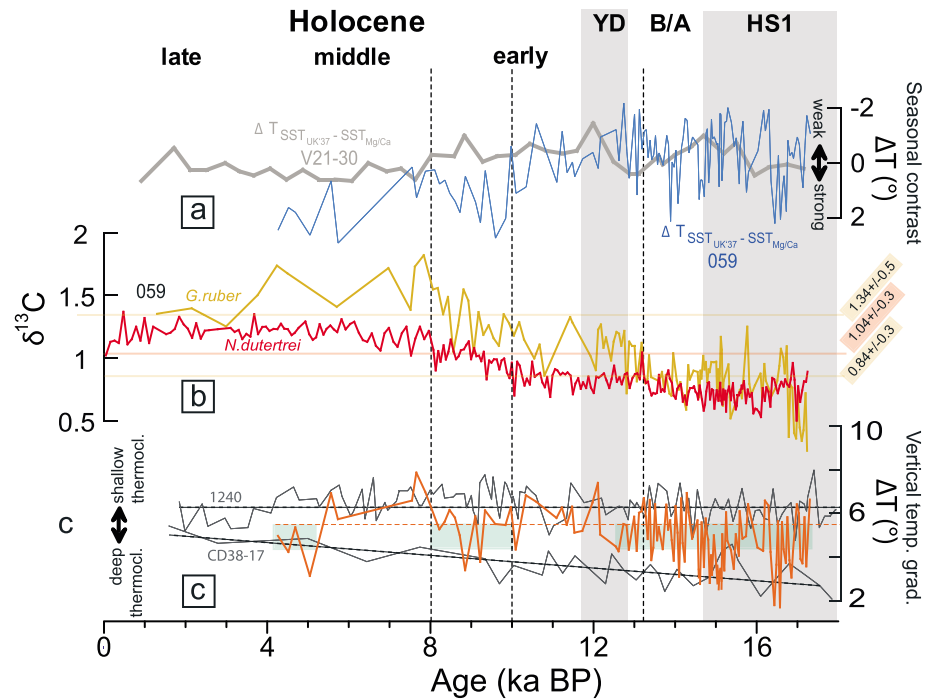
Figure 6. Changes in thermocline depth, seasonal contrast, and planktonic foraminiferal $\delta^{13}C$. (a) Record of seasonal contrast within the Gulf of Guayaquil indicated by the difference between $SST_{UK'37}$ and $SST_{Mg/Ca}$ of core 059 ($SST_{Mg/Ca}$-$SST_{UK'37}$, light blue, presented as deviation from the ~17.3 kyr mean) in comparison to the according data set of EEP core V21-30 (gray) (raw data from *Koutavas and Joanides* [2012] and *Koutavas and Sachs* [2008]). (b) The $\delta^{13}C$ of *G. ruber* and *N. dutertrei* of core 059. The horizontal lines provide average $\delta^{13}C$ of core-top *G. ruber* from either north or south of 5°S off Peru (yellow, lower and upper lines, respectively), and $\delta^{13}C$ of *N. dutertrei* (red) (compare to Figure 1 and the supporting information). (c) Changes of the thermocline depth at core location 059 (orange), ODP Site 1240 (gray [*Pena et al.*, 2008]) and core CD38-17 (gray [*Sadekov et al.*, 2013]), calculated from the difference ΔT between $SST_{Mg/Ca}$ (*G. ruber*) and $subSST_{Mg/Ca}$ (*N. dutertrei*). The linear regression lines are stippled. Small (large) ΔT points to deep (shallow) thermocline. The light greenish bands denote prominent time periods of thermocline deepening. The gray shaded areas denote the deglacial cool intervals Heinrich Stadial 1 (HS1) and Younger Dryas (YD).

Holocene $SST_{Mg/Ca}$ is close to the modern austral winter (JAS) temperature condition (Figure 4a). In support of our notion on the seasonal preference of proxies, the annual Holocene SST estimate (SST_{annual}) averaged from both $SST_{UK'37}$ and $SST_{Mg/Ca}$ [see *Timmermann et al.*, 2014] is close to the modern annual SST [*Locarnini et al.*, 2010] (Figure 4b).

The seasonal contrast (expressed as $\Delta T_{SSTUK'37 - SSTMg/Ca}$ in Figure 6a, in accordance with *Timmermann et al.* [2014]) was lowest although established during the deglaciation. The core 059 $SST_{UK'37}$ and $SST_{Mg/Ca}$ records are *quasi* identical in absolute temperature and amplitude during the deglaciation until the onset of the Holocene (Figure 4a), implying that the growth season of alkenones was longer than today and living conditions for *G. ruber* became optimal nearly year-round. Since ~10 ka B.P., $SST_{Mg/Ca}$ values remain on average lower than alkenone temperature estimates, superimposed by a pronounced cooling of ~2°C in the *G. ruber* signal. The ongoing Holocene is characterized by diverging $SST_{Mg/Ca}$ and $SST_{UK'37}$ records: cooling in $SST_{Mg/Ca}$ toward values prevailing during HS1 and gradually increasing $SST_{UK'37}$ temperatures. The difference between $SST_{UK'37}$ and $SST_{Mg/Ca}$ increases to ~2°C during the Holocene (Figure 4a). The increasing seasonal contrast since ~10 ka (Figure 6a) implies a gradually increasing influence of coastal upwelling at our core locations off Peru: coccolithophorid growth and hence, alkenone production favored by water column stratification became successively restricted to the nonupwelling austral summer season, and $SST_{UK'37}$ increased. Instead, foraminiferal $SST_{Mg/Ca}$ decreased during the course of the Holocene (Figure 4a). Since ~4 ka living conditions for *G. ruber* became unfavorable leading to very low abundances of *G. ruber* at our core locations. Even though our core locations are located north of the modern Peruvian upwelling center, we suspect that the northward expansion and strengthening of austral winter upwelling might have influenced our core locations particularly strongly since ~4 ka B.P. The modern coastal

upwelling off Peru is supposed to be shallow (maximum 75–100 m deep) [*Huyer*, 1980; *Huyer et al.*, 1987] and in fact affects the living depth of *G. ruber* rather than that of *N. dutertrei*. *Thiede* [1983] and *Ibaraki* [1990] noted that *G. ruber* is rarely found in upwelling areas. Congruently, otolith $\delta^{18}O$ data point to sea surface cooling related to enhanced upwelling off Peru after ~5 ka B.P. [*Andrus et al.*, 2002].

In contrast to the Gulf of Guayaquil, the growing seasonal contrast is not reflected at EEP Site V21-30 close to the Galapagos Islands (Figure 6a). Here the deglacial to Holocene $SST_{Mg/Ca}$ and $SST_{UK'37}$ records develop concordantly, showing only a modest warming of maximum ~1.5°C [*Koutavas and Sachs*, 2008; *Koutavas and Joanides*, 2012]. Also, none of the available $SST_{Mg/Ca}$ records from the EEP (ODP Site 1240 [*Pena et al.*, 2008], core TR163-22 [*Lea et al.*, 2006], and core CD38-17 [*Sadekov et al.*, 2013]) is showing the rapid cooling at ~10 ka B.P. as is observed in the Gulf of Guayaquil (Figure 5a). Apparently, core 059 is increasingly affected by the seasonally skewed (austral winter) northward expansion of CCW since ~10 ka B.P. This expansion took place in line with the strengthening of the Southeast Trades, the rapid recession of warm ESW/TSW in conjunction with a preferential northern position of the EF, and the beginning impact of seasonal upwelling processes. Synchronous to the oceanographic change in the Gulf of Guayaquil at ~10 ka B.P., the opposing $SST_{Mg/Ca}$ trends from further northwest in the EEP north of the equator (ODP Site 1240: relative warming; core TR163-22: relative cooling) (Figure 5a) suggest a rather differential spatial development of the EF between core locations.

The augmented presence of warmer ESW expanding further southward toward the Gulf of Guayaquil than today and replacing the CCW, instead, is reconstructed for the Bølling Interstadial and the time period from ~12.5–10 ka B.P. (YD and early Holocene) (Figure 5) when Southeast Trades were weaker and coastal upwelling off Peru was reduced and/or shifted further to the south [e.g., *Streten and Zillman*, 1984; *Mollier-Vogel*, 2013].

4.4. Vertical Temperature Gradient Reflects Thermocline Change

The interaction of both sea surface and subsurface waters is crucial for the water column structure and thermocline development in the Gulf of Guayaquil. Notably, the oceanographic deglacial to Holocene developments at different depth levels are driven by rather different processes. The large-amplitude sea surface dweller *G. ruber* $\delta^{18}O$ signal (~2.5‰) intimately captures the deglacial two-step northern hemisphere climate pattern [*NGICP Members*, 2004] (Figure 2a) and is congruent to the ODP Site 1240 and core CD38-17 $\delta^{18}O_{G.ruber}$ records (Figure S3f). In particular, the presence of Heinrich Event 1, the Younger Dryas, and the millennial-scale Dansgaard-Oeschger climate events during the last glacial were already described in the surface EEP by *Kienast et al.* [2006], *Pahnke et al.* [2007], *Koutavas et al.* [2006], and *Dubois et al.* [2014]. The subsurface oceanographic development, in contrast, neither reveals the northern hemisphere deglacial to Holocene climate pattern nor the clear reflection of the Southern Hemisphere climate signal (see section 4.1).

The interdynamics between surface and subsurface water masses are best reflected in the temporal development of the thermal structure and hence, stratification of the upper ocean, which is inferred from the difference between $SST_{Mg/Ca}$ and $subSST_{Mg/Ca}$ at the respective core locations. Large (small) vertical temperature differences ΔT (here: $SST_{Mg/Ca}$–$subSST_{Mg/Ca}$; cf. Figure 6c) are interpreted as a shallow (deep) thermocline [e.g., *Steph et al.*, 2009], provided that the foraminiferal species that the temperature information is derived from did not change habitat over time. We consider here that *G. ruber* did not change habitat significantly over time, as it is a very shallow dwelling, symbiont-bearing species dependant on high light levels. The possibility that *N. dutertrei* changed habitat was considered cautiously (see supporting information), and we stay with our notion of an overall deep *N. dutertrei* habitat of ~150–200 over time at our core locations (see section 3.2.2). We are aware that *Pena et al.* [2008] and *Sadekov et al.* [2013] assume a shallower habitat for *N. dutertrei* at ODP Site 1240 and core CD38-17 [*Sadekov et al.*, 2013], respectively.

The vertical ΔT at core location 059 varies considerably between ~2-8°C (mean $\Delta T = 4.7°C$, ~1.5°C standard deviation) (Figure 6c). A preferentially small ΔT, hence a deep thermocline, persisted during HS 1 and large parts of the B/A until ~13 ka B.P., during ~10–8 ka B.P., and during ~5.5–4 ka B.P. Further offshore, the upper ocean thermal structure developed differently. The vertical gradients ΔT are half as large at ODP Site 1240 (~5–8°C) and at core CD38-17 (~2.5–5.5°C), with either no considerable change over time or gradual

shoaling of the thermocline (Figure 6c). It might be speculated in this respect that the thermocline development at core location CD38-17 (1°36.04′S, 90°25.32′W) might have been caused by the continuously strengthened eastward flow of the EUC. *Karnauskas et al.* [2012] provides evidence that close to the Galapagos Islands the EUC is centered between the equator and 0.5°S today. EUC partly upwells on the western side of the Galapagos and bifurcates into a shallow southern and deeper northern core, both of which continue eastward and reach the Peruvian coast. From this perspective it seems reasonable that the core location CD38-17 is revealing a change in thermocline, while ODP Site 1240 is not.

In the Gulf of Guayaquil, the time period at ~17.3–13 ka B.P. is marked by an overall deep although highly variable thermocline and a weakly developed seasonal contrast. The low $\delta^{13}C$ values of *G. ruber* and *N. dutertrei* are rather similar (Figure 6b), pointing to a stratified low productive upper ocean. The $\delta^{13}C_{G.ruber}$ values compare to the modern $\delta^{13}C_{G.ruber}$ values of 0.84 ± 0.3‰ from outside the today's coastal upwelling area off Peru (see supporting information). These data and the perennially warm and saline conditions at subsurface level coming close to sea surface conditions imply that EUC-sourced ESSW inflow similar to today did not take place off Peru, but that ESSW was replaced by ESW expanding vertically and warming the subsurface ocean layers "from above."

After ~13 ka B.P. until ~10 ka, ΔT gradually increased, the $\delta^{13}C$ values of *G. ruber* and *N. dutertrei* started to deviate from each other, and the seasonal contrast strengthened, implying pronounced oceanographic and climatic reorganizations (Figure 6). With the exception of distinct periods during ~10–8 ka B.P., ~5.5–4 ka B.P., and most likely ~0.5–1.5 ka B.P. (surface data are missing here), the Holocene is characterized by a large vertical ΔT, which comes close to the modern ΔT of 7°C at the core location between ~30 m (~21°C) and ~200 m water depth (~14°C) [*Locarnini et al.*, 2010] and points to a rather shallow thermocline depth. The $\delta^{13}C_{G.ruber}$ values compare to values, which today are only found in core-top samples from south of 5°S in the highly-productive coastal upwelling area off Peru, and remain heavier by ~0.5‰ than for *N. dutertrei* (Figure 6b). All proxy data point to the relatively increasing presence of northward propagating, cool and nutrient-rich CCW during the Holocene in line with a northern position of the ITCZ, strengthened Southeast Trades, and gradually evolving shallow coastal upwelling south of our core locations (Figure 6). At the same time, ESSW gradually invades at subsurface level into the Gulf of Guayaquil, caused by the strengthened EUC flow. As the seasonal contrast is well established after ~10 ka B.P. (Figure 6a), we conclude that the variations in thermocline depth during the Holocene rather relate to the austral winter (JAS) season.

The close interplay between CCW at the sea surface and ESSW at subsurface level controlling the thermocline becomes in particular obvious during ~10–8 ka B.P., ~5.5–4 ka B.P., and most likely ~0.5–1.5 ka B.P. Considerable warming at subsurface level by ~2°C at rather cool surface conditions leads to an overall small vertical ΔT, hence to the relative deepening of the thermocline (Figure 6c). During these Holocene time intervals, ESSW is displaced by warm tropical waters, most likely ESW, implying clear and short-term interruptions in EUC strength and flow. Insofar, the ESSW and hence the EUC are intermittent and nonsteady features off Peru during the Holocene. We are aware, in this respect, that our Holocene reconstuction suffers from the partially low abundances of *G. ruber* in core 059.

Model experiments of *Drenkard and Karnauskas* [2014] suggest that the EUC strengthening may be explained by the strengthening of the W Pacific easterly trade winds leading to an increased oceanic zonal pressure gradient during austral autumn. Similarly, the weakening of the E Pacific trade winds during austral winter causes the flattening of zonal pressure gradients and the weakening of surface currents, hence a slowdown of the Pacific Walker circulation, but reduces the EUC deceleration through vertical friction.

Other studies invoke off-equatorial mechanisms for EUC strengthening [*Luo et al.*, 2009; *Sen Gupta et al.*, 2012], such as the strengthening of western boundary currents. From theoretical considerations *Liu et al.* [2000] concluded that changes in the equatorial thermocline might be driven by water mass subduction processes in the Southern Ocean the way that source and/or properties of water masses traveling with the EUC changed. Various lines of evidence stress the notion on a Southern Ocean—EEP thermocline teleconnection. A low- to high-latitude accordance of proxy records was noted already by *Lea et al.* [2006] from the Galapagos region and was explained by a direct ocean link via subduction of intermediate and mode waters in the Southern Ocean and subsequent resurfacing in the EEP after a long transit within the EUC. From their ODP Site 1240 deep-dweller planktonic foraminiferal ε_{Nd} record, *Pena et al.* [2013] claimed

that the EUC received stronger contributions of intermediate southern component waters via "oceanic tunneling" mainly during the cool climate periods HS2, Last Glacial Maximum, HS1, and Preboral to Holocene. Alternatively and/or in tandem with the oceanic link, both Antarctica and the EEP might have responded simultaneously to greenhouse forcing (i.e., atmospheric CO_2) [*Koutavas et al.*, 2006]. Most likely, multiple oceanic-atmospheric drivers contributed to the changing equatorial Pacific circulation pattern.

5. Conclusions

Our marine multiproxy data series from the Gulf of Guayaquil (northern Peru) covering the last ~17.3 kyr reveal the deglacial to Holocene development of the hydrographically complex easternmost Eastern Equatorial Pacific. The subsurface development at ~150–200 m water depth is inferred from the planktonic foraminifer *N. dutertrei* (isotope) geochemical signature, reflecting changes in subsurface temperature, salinity, and nutrient conditions. Similar surface ocean parameters are derived from the (isotope) geochemical signature of the surface-dwelling *G. ruber* and alkenones.

The deglacial pattern of sea surface change retraces the northern hemisphere climate signal emphasizing the importance of high northern latitude climate processes for the tropical surface ocean close to Peru. The oceanographic development at sea surface, however, is different from the EEP further offshore, reflecting an intimate, seasonally skewed interrelationship between CCW and ESW/TSW. In particular since ~10 ka, CCW becomes rapidly and sustainedly present in the Gulf of Guayaquil, while ESW is displaced and TSW moves northward in line with the northward moving EF and the ITCZ. At the same time, the seasonal contrast as indicated by the different developments of alkenone and foraminiferal Mg/Ca-based SST proxies, prominently evolves implying that the CCW/ESW interaction in the Gulf of Guayaquil mainly operates during the austral winter season. The increasing seasonal contrast since ~10 ka B.P. further implies that coastal upwelling off Peru gradually intensified and expanded northward, affecting the Gulf of Guayaquil core locations most intensively since 4 ka B.P. in response to a seasonally changing atmospheric circulation pattern (Southeast Trades).

At subsurface, the presence of EUC-sourced ESSW in the Gulf of Guayaquil is continuously growing, most prominently since ~10–8 ka. Before, during HS1 and large parts of the B/A and similarly during short Holocene time intervals at ~5.1–4 ka B.P. and ~1.5–0.5 ka B.P., the admixture of ESSW was reduced most likely in response to both short-term weakening of EUC strength and flow from the northwest and emplacement by tropical ESW considerably warming the uppermost ocean layers.

Modeling [*Timmermann et al.*, 1999; *Liu et al.*, 2000, 2014] and observations [*Trenberth and Hoar*, 1996] suggested that thermocline conditions might be sensitive to ENSO and hence, preconditioning of ENSO might originate from outside the tropics. Our proxy data addressing the close interaction between sea surface CCW and subsurface EUC-sourced ESSW are not finally conclusive in this respect but may enrich the still ongoing discussion on ENSO forcing.

References

Andrus, C. F. T., D. E. Crowe, D. H. Sandweiss, E. J. Reitz, and C. S. Romanek (2002), Otolith $\delta^{18}O$ record of mid-Holocene sea surface temperatures in Peru, *Science*, 295(5559), 1508–1511, doi:10.1126/science.1062004.

Antonov, J. I., D. Seidov, T. P. Boyer, R. A. Locarnini, A. V. Mishonov, H. E. Garcia, O. K. Baranova, M. M. Zweng, and D. R. Johnson (2010), World Ocean Atlas 2009, Volume 2: Salinity, in *NOAA Atlas NESDIS*, vol. 69, edited by S. Levitus, p. 184, U.S. Gov. Print. Off., Washington, D. C.

Austermann, J., J. X. Mitrovica, K. Latychev, and G. A. Milne (2013), Barbados-based estimate of ice volume at Last Glacial Maximum affected by subducted plate, *Nat. Geosci.*, 6(7), 553–557, doi:10.1038/ngeo1859.

Ayón, P., M. I. Criales-Hernandez, R. Schwamborn, and H.-J. Hirche (2008), Zooplankton research off Peru: A review, *Prog. Oceanogr.*, 79(2–4), 238–255, doi:10.1016/j.pocean.2008.10.020.

Bahr, A., D. Nürnberg, C. Karas, and J. Grützner (2013), Millennial-scale versus long-term dynamics in the surface and subsurface of the western North Atlantic Subtropical Gyre during marine isotope stage 5, *Global Planet. Change*, 111, 77–87, doi:10.1016/j.gloplacha.2013.08.013.

Barker, S., G. Knorr, M. Vautravers, P. Diz, and L. C. Skinner (2010), Extreme deepening of the Atlantic overturningcirculation during deglaciation, *Nat. Geosci.*, 3, 567–571, doi:10.1038/NGEO921.

Brink, K. H., D. Halpern, A. Huyer, and R. L. Smith (1983), The physical environment of the Peruvian upwelling system, *Prog. Oceanogr.*, 12(3), 285–305, doi:10.1016/0079-6611(83)90011-3.

Cane, M. A. (2005), The evolution of El Niño, past and future, *Earth Planet. Sci. Lett.*, 230(3–4), 227–240, doi:10.1016/j.epsl.2004.12.003.

Chaigneau, A., N. Dominguez, G. Eldin, L. Vasquez, R. Flores, C. Grados, and V. Echevin (2013), Near-coastal circulation in the Northern Humboldt Current System from shipboard ADCP data, *J. Geophys. Res. Oceans*, 118, 5251–5266, doi:10.1002/jgre.20328.

Czeschel, R., L. Stramma, F. U. Schwarzkopf, B. S. Giese, A. Funk, and J. Karstensen (2011), Middepth circulation of the eastern tropical South Pacific and its link to the oxygen minimum zone, *J. Geophys. Res.*, 116, C01015, doi:10.1029/2010JC006565.

Drenkard, E. J., and K. B. Karnauskas (2014), Strengthening of th Pacific Equatorial Undercurrent in the SODA Reanalysis: Mechanisms, Ocean Dynamics, and Implications, *J. Clim.*, *27*, 2405–2416, doi:10.1175/JCLI-D-13-00359.1.

Dubois, N., M. Kienast, C. Normandeau, and T. D. Herbert (2009), Eastern equatorial Pacific cold tongue during the Last Glacial Maximum as seen from alkenone paleothermometry, *Paleoceanography*, *24*, PA4207, doi:10.1029/2009PA001781.

Dubois, N., M. Kienast, S. Kienast, S. Calvert, R. Francois, and R. F. Anderson (2010), Sedimentary opal records in the eastern equatorial Pacific: It is not all about leakage, *Global Biogeochem. Cycles*, *24*, GB4020, doi:10.1029/2010GB003821.

Dubois, N., M. Kienast, S. Kienast, and A. Timmermann (2014), Millennial-scale Atlantic/East Pacific sea surface temperature linkages during the last 100,000 years, *Eath Planet. Sci. Lett.*, *396*, 134–142, doi:10.1016/j.epsl.2014.04.008.

EPICA Community Members (2006), One-to-one coupling of glacial climate variability in Greenland and Antarctica, *Nature*, *444*(9), 195–198, doi:10.1038/nature05301.

Fiedler, P. C., and L. D. Talley (2006), Hydrography of the eastern tropical Pacific: A review, *Prog. Oceanogr.*, *69*(2–4), 143–180, doi:10.1016/j.pocean.2006.03.008.

Goñi, M. A., D. M. Hartz, R. C. Thunell, and E. Tappa (2001), Oceanographic considerations for the application of the alkenone-based paleotemperature $U^{K'}_{37}$ index in the Gulf of California, *Geochim. Cosmochim. Acta*, *65*(4), 545–557, doi:10.1016/S0016-7037(00)00559-7.

Goodman, P. J., W. Hazeleger, P. de Vries, and M. Cane (2005), Pathways into the Pacific Equatorial Undercurrent: A Trajectory Analysis, *J. Phys. Oceanogr.*, *35*(11), 2134–2151, doi:10.1175/JPO2825.1.

Greaves, M., et al. (2008), Interlaboratory comparison study of calibration standards for foraminiferal Mg/Ca thermometry, *Geochem. Geophys. Geosyst.*, *9*, Q08010, doi:10.1029/2008GC001974.

Huyer, A. (1980), The offshore structure and subsurface expression of sea level variations off Peru, 1976–1977, *J. Phys. Oceanogr.*, *10*, 1755–1768.

Huyer, A., R. L. Smith, and T. Paluszkiewicz (1987), Coastal upwelling off Peru during normal and El Niño times, 1981–1984, *J. Geophys. Res.*, *92*(C13), 14,297–14,307, doi:10.1029/JC092iC13p14297.

Ibaraki, M. (1990), Eocene through Pleistocene planktonic foraminifers off Peru, Leg 112—Biostratigraphy and paleoceanography, in *Proceedings of the Ocean Drilling Program*, *Scientific Results*, vol. 112, pp. 239–262, Ocean Drilling Program, College Station, Tex., doi:10.2973/odp.proc.sr.112.197.1990.

Karnauskas, K. B., R. Murtugudde, and A. J. Busalacchi (2010), Observing the Gálapagos-EUC interaction: Insights and challenges, *J. Phys. Oceanogr.*, *40*, 2768–2777, doi:10.1175/2010JPO4461.1.

Karstensen, J., and O. Ulloa (2008), Peru–Chile Current System, in *Encyclopedia of Ocean Sciences*, edited by J. H. Steele, K. K. Turekian, and S. A. Thorpe, pp. 385–392, Elsevier, Amsterdam.

Kessler, W. S. (2006), The circulation of the eastern tropical Pacific: A review, *Prog. Oceanogr.*, *69*(2–4), 181–217, doi:10.1016/j.pocean.2006.03.009.

Kienast, M., S. S. Kienast, S. E. Calvert, T. I. Eglinton, G. Mollenhauer, R. Francois, and A. C. Mix (2006), Eastern Pacific cooling and Atlantic overturning circulation during the last deglaciation, *Nature*, *443*(7113), 846–849, doi:10.1038/nature05222.

Kienast, S. S., T. Friedrich, N. Dubois, P. S. Hill, A. Timmermann, A. C. Mix, and M. Kienast (2013), Near collapse of the meridional SST gradient in the eastern equatorial Pacific during Heinrich Stadial 1, *Paleoceanography*, *28*, 663–674, doi:10.1002/2013PA002499.

Klostermann, L. (2011), Hydrography and stable isotopes (oxygen, carbon) in water masses off Peru and Ecuador MSc thesis, Univ. Kiel, 49 pp.

Koutavas, A., and J. P. Sachs (2008), Northern timing of deglaciation in the eastern equatorial Pacific from alkenone paleothermometry, *Paleoceanography*, *23*, PA4205, doi:10.1029/2008PA001593.

Koutavas, A., and S. Joanides (2012), El Niño-Southern Oscillation extrema in the Holocene and Last Glacial Maximum, *Paleoceanography*, *27*, PA4208, doi:10.1029/2012PA002378.

Koutavas, A., P. B. de Menocal, G. C. Olive, and J. Lynch-Stieglitz (2006), Mid-Holocene El Niño–Southern Oscillation (ENSO) attenuation revealed by individual foraminifera in eastern tropical Pacific sediments, *Geology*, *34*(12), 993–996, doi:10.1130/g22810a.1.

Lea, D. W., D. K. Pak, and H. J. Spero (2000), Climate impact of late Quaternary equatorial Pacific sea surface temperature variations, *Science*, *289*(5485), 1719–1724, doi:10.1126/science.289.5485.1719.

Lea, D. W., D. K. Pak, C. L. Belanger, H. J. Spero, M. A. Hall, and N. J. Shackleton (2006), Paleoclimate history of Gálapagos surface waters over the last 135,000 yr, *Quat. Sci. Rev.*, *25*(11–12), 1152–1167, doi:10.1016/j.quascirev.2005.11.010.

Leduc, G., L. Vidal, O. Cartapanis, and E. Bard (2009), Modes of eastern equatorial Pacific thermocline variability: Implications for ENSO dynamics over the last glacial period, *Paleoceanography*, *24*, PA3202, doi:10.1029/2008PA001701.

Leduc, G., R. Schneider, J.-H. Kim, and G. Lohmann (2010), Holocene and Eemian sea surface temperature trends as revealed by alkenone and Mg/Ca paleothermometry, *Quat. Sci. Rev.*, *29*(7–8), 989–1004.

Liu, Z., J. Kutzbach, and L. Wu (2000), Modeling climate shift of El Niño variability in the Holocene, *Geophys. Res. Lett.*, *27*(15), 2265–2268, doi:10.1029/2000GL011452.

Liu, Z., Z. Lu, X. Wen, B. L. Otto-Bliesner, A. Timmermann, and K. M. Cobb (2014), Evolution and forcing mechanisms of El Niño over the past 21,000 years, *Nature*, *515*, 550–553, doi:10.1038/nature13963.

Locarnini, R. A., A. V. Mishonov, J. I. Antonov, T. P. Boyer, H. E. Garcia, O. K. Baranova, M. M. Zweng, and D. R. Johnson (2010), World Ocean Atlas 2009, Volume 1: Temperature, in *NOAA Atlas NESDIS*, vol. 68, edited by S. Levitus, p. 184, U.S. Gov. Print. Off., Washington, D. C.

Loubere, P., M. Richaud, Z. Liu, and F. Mekik (2003), Oceanic conditions in the eastern equatorial Pacific during the onset of ENSO in the Holocene, *Quat. Res.*, *60*(2), 142–148, doi:10.1016/S0033-5894(03)00092-9.

Lukas, R. (1986), The termination of the Equatorial Undercurrent in the eastern Pacific, *Prog. Oceanogr.*, *16*(2), 63–90, doi:10.1016/0079-6611(86)90007-8.

Luo, Y., L. M. Rothstein, and R.-H. Zhang (2009), Response of the Pacific subtropical-thermocline water pathways and transports to global warming, *Geophys. Res. Lett.*, *36*, L04601, doi:10.1029/2008GL036705.

McPhaden, M. J., et al. (1998), The tropical ocean-global atmosphere observing system: A decade of progress, *J. Geophys. Res.*, *103*(C7), 14,169–14,240, doi:10.1029/97JC02906.

Mollier-Vogel, E., G. Leduc, T. Böschen, P. Martinez, and R. R. Schneider (2013), Rainfall response to orbital and millennial forcing in northern Peru over the last 18 ka, *Quat. Sci. Rev.*, *76*, 29–38, doi:10.1016/j.quascirev.2013.06.021.

Monnin, E., A. Indermühle, A. Dällenbach, J. Flückiger, B. Stauffer, T. F. Stocker, D. Raynaud, and J. M. Barnola (2001), Atmospheric CO_2 concentrations over the last glacial termination, *Science*, *291*, 112–114.

Montes, I., F. Colas, X. Capet, and W. Schneider (2010), On the pathways of the equatorial subsurface currents in the eastern equatorial Pacific and their contributions to the Peru-Chile Undercurrent, *J. Geophys. Res.*, *115*, C09003, doi:10.1029/2009JC005710.

NGICP Members (2004), High-resolution record of Northern Hemisphere climate extending into the last interglacial period, *Nature*, *431*(7005), 147–151, doi:10.1038/nature02805.

Nürnberg, D. (2000), Taking the temperature of past ocean surfaces, *Science*, 289(5485), 1698–1699, doi:10.1126/science.289.5485.1698.

Nürnberg, D., M. Ziegler, C. Karas, R. Tiedemann, and M. Schmidt (2008), Interacting loop current variability and Mississippi River discharge over the past 400 kyr, *Earth Planet. Sci. Lett.*, 272(1/2), 278–289, doi:10.1016/j.epsl.2008.04.051.

Nürnberg, D., Bahr, A., Mildner, T., Eden, C. (2015) Loop current variability—Its relation to meridional overturning circulation and the impact of Mississippi discharge, in *Integrated Analysis of Interglacial Climate Dynamics, Springer Briefs in Earth Syst. Sci.*, edited by M. Schulz, and A. Paul, pp. 55–62, Springer International, Cham, doi:10.1007/978-3-319-00693-2.

Pahnke, K., J. P. Sachs, L. Keigwin, A. Timmermann, and S.-P. Xie (2007), Eastern tropical Pacific hydrologic changes during the past 27,000 years from D/H ratios in alkenones, *Paleoceanography*, 22, PA4214, doi:10.1029/2007PA001464.

Pak, H., and J. R. V. Zanefeld (1974), Equatorial Front in the East Pacific Ocean, *J. Phys. Oceanogr.*, 4, 570–578.

Palacios, D. M. (2004), Seasonal patterns of sea-surface temperature and ocean color around the Galápagos: Regional and local influences, *Deep Sea Res. Part II: Topical Studies in Oceanography*, 51(1–3), 43–57, doi:10.1016/j.dsr2.2003.08.001.

Pena, L. D., E. Calvo, I. Cacho, S. Eggins, and C. Pelejero (2005), Identification and removal of Mn-Mg-rich contaminant phases on foraminiferal tests: Implications for Mg/Ca past temperature reconstructions, *Geochem. Geophys. Geosyst.*, 6, Q09P02, doi:10.1029/2005GC000930.

Pena, L. D., I. Cacho, P. Ferretti, and M. A. Hall (2008), El Niño-Southern Oscillation-like variability during glacial terminations and interlatitudinal teleconnections, *Paleoceanography*, 23, PA3101, doi:10.1029/2008PA001620.

Pena, L. D., S. L. Goldstein, S. R. Hemming, K. M. Jones, E. Calvo, C. Pelejero, and I. Cacho (2013), Rapid changes in meridional advection of Southern Ocean intermediate waters to the tropical Pacific during the last 30 kyr, *Earth Planet. Sci. Lett.*, 368, 20–32, doi:10.1016/j.epsl.2013.02.028.

Penven, P., V. Echevin, J. Pasapera, F. Colas, and J. Tam (2005), Average circulation, seasonal cycle, and mesoscale dynamics of the Peru Current System: A modeling approach, *J. Geophys. Res.*, 110, C10021, doi:10.1029/2005JC002945.

Pfannkuche, O., M. Frank, R. Schneider, and L. Stramma (2011), *Climate-Biogeochemistry Interactions in the Tropical Ocean of the SE-American Oxygen Minimum Zone*, edited by L. D. Forschungsschiffe, 200 pp., Institut für Meereskunde der Univ. Hamburg, Hamburg.

Philander, S. G. H. (1983), El Niño Southern Oscillation phenomena, *Nature*, 302(5906), 295–301, doi:10.1038/302295a0.

Prahl, F. G., J. F. Rontani, N. Zabeti, S. E. Walinsky, and M. A. Sparrow (2010), Systematic pattern in $U^{K'37}$ - Temperature residuals for surface sediments from high latitude and other oceanographic settings, *Geochim. Cosmochim. Acta*, 74(1), 131–143, doi:10.1016/j.gca.2009.09.027.

Regenberg, M., S. Steph, D. Nürnberg, R. Tiedemann, and D. Garbe-Schönberg (2009), Calibrating Mg/Ca ratios of multiple planktonic foraminiferal species with δ^{18}O-calcification temperatures: Paleothermometry for the upper water column, *Earth Planet. Sci. Lett.*, 278, 324–336.

Rincón-Martínez, D., F. Lamy, S. Contreras, G. Leduc, E. Bard, C. Saukel, T. Blanz, A. Mackensen, and R. Tiedemann (2010), More humid interglacials in Ecuador during the past 500 kyr linked to latitudinal shifts of the equatorial front and the Intertropical Convergence Zone in the eastern tropical Pacific, *Paleoceanography*, 25, PA2210, doi:10.1029/2009PA001868.

Rodgers, K. B., B. Blanke, G. Madec, O. Aumont, P. Ciais, and J.-C. Dutay (2003), Extratropical sources of Equatorial Pacific upwelling in an OGCM, *Geophys. Res. Lett.*, 30(2), 1084, doi:10.1029/2002GL016003.

Rubin, S., J. G. Goddard, D. W. Chipman, T. Takahashi, S. C. Sutherland, J. L. Reid, J. H. Swift, L. D. Talley, and A. Kozyr (1998), *Carbon Dioxide, Hydrographic, and Chemical Data Obtained in the South Pacific Ocean (WOCE Sections P16A/P17A, P17E/P19S, and P19C, R/V Knorr, October 1992-April 1993)*, p. 186, Carbon Dioxide Information Analysis Center, Oak Ridge Natl. Lab., U.S. Dep. of Energy, Oak Ridge, Tenn.

Sadekov, A. Y., R. Ganeshram, L. Pichevin, R. Berdin, E. McClymont, H. Elderfield, and A. W. Tudhope (2013), Paleoclimate reconstructions reveal a strong link between El Niño-Southern Oscillation and Tropical Pacific mean state, *Nat. Commun.*, 4, 2692, doi:10.1038/ncomms3692.

Sandweiss, D. H., J. B. Richardson, E. J. Reitz, H. B. Rollins, and K. A. Maasch (1996), Geoarchaeological Evidence from Peru for a 5000 Years B.P. Onset of El Niño, *Science*, 273(5281), 1531–1533, doi:10.1126/science.273.5281.1531.

Schlitzer, R. (2010), Ocean data view. [Available at http://odv.awi.de.]

Schneider, B., G. Leduc, and W. Park (2010), Disentangling seasonal signals in Holocene climate trends by satellite-model-proxy integration, *Paleoceanography*, 25, PA4217, doi:10.1029/2009PA001893.

Sen Gupta, A., A. Ganachaud, S. McGregor, J. N. Brown, and L. Muir (2012), Drivers of the projected changes to the Pacific Ocean equatorial circulation, *Geophys. Res. Lett.*, 39, L09605, doi:10.1029/2012GL051447.

Silva, N., N. Rojas, and A. Fedele (2009), Water masses in the Humboldt Current System: Properties, distribution, and the nitrate deficit as a chemical water mass tracer for Equatorial Subsurface Water off Chile, *Deep Sea Res., Part II Topical Studies in Oceanography*, 56(16), 1004–1020, doi:10.1016/j.dsr2.2008.12.013.

Steph, S., M. Regenberg, R. Tiedemann, S. Mulitza, and D. Nürnberg (2009), Stable isotopes of planktonic foraminifera from tropical Atlantic/Caribbean coretops: Implications for reconstructing upper ocean stratification, *Mar. Micropaleontol.*, 71, 1–19, doi:10.1016/j.marmicro.2008.12.004.

Streten, N. A., and J. W. Zillman (1984), Climate of the South Pacific Ocean, in *World Survey of Climatology - Volume 15: Climates of the Oceans*, edited by H. van Loon, pp. 263–430, Elsevier, Amsterdam, Oxford, New York, Tokyo.

Strub, P. T., J. M. Mesias, and C. James (1995), Altimeter observations of the Peru-Chile Countercurrent, *Geophys. Res. Lett.*, 22(3), 211–214, doi:10.1029/94GL02807.

Strub, P. T., J. M. Mesías, V. Montecino, J. Rutllant, and S. Salinas (1998), Coastal ocean circulation off Western South America, in *The Sea - Volume 11*, vol. 11, edited by A. R. Robinson and K. H. Brink, pp. 273–313, John Wiley, New York.

Thiede, J. (1983), Skeletal plankton and nekton in upwelling water masses off northwestern South America and Northwest Africa, in *Coastal Upwelling: Its Sediment Record, Part A. Responses of the Stratigr.*, edited by E. Suess and J. Thiede, pp. 263–314, Cambridge Univ. Press, Cambridge.

Thompson, L. G., E. Mosley-Thompson, M. E. Davis, P.-N. Lin, K. A. Henderson, J. Cole-Dai, J. F. Bolzan, and K.-b. Liu (1995), Late glacial stage and Holocene tropical ice core records from Huascaran, Peru, *Science*, 269, 46–50.

Thunell, R., E. Tappa, C. Pride, and E. Kincaid (1999), Sea-surface temperature anomalies associated with the 1997–1998 El Niño recorded in the oxygen isotope composition of planktonic foraminifera, *Geology*, 27(9), 843–846, doi:10.1130/0091-7613.

Timmermann, A., J. Oberhuber, A. Bacher, M. Esch, M. Latif, and E. Roeckner (1999), Increased El Nino frequency in a climate model forced by future greenhouse warming, *Nature*, 398, 694–697.

Timmermann, A., J. Sachs, and O. Elison Timm (2014), Assessing the divergent SST behaviour during the last 21 ka derived from alkenones and *G. ruber*-Mg/Ca in the equatorial Pacific, *Paleoceanography*, 29, 680–696, doi:10.1002/2013PA002598.

Toggweiler, J. R., K. Dixon, and W. S. Broecker (1991), The Peru upwelling and the ventilation of the South Pacific thermocline, *J. Geophys. Res.*, 96(C11), 20,467–20,497, doi:10.1029/91JC02063.

Trenberth, K., and T. Hoar (1996), The 1990–1995 El Nino-Southern Oscillation event: Longest on record, *Geophys. Res. Lett.*, *23*(1), 57–60, doi:10.1029/95GL03602.

Tsuchiya, M., and L. D. Talley (1998), A Pacific hydrographic section at 88°W: Water property distribution, *J. Geophys. Res.*, *103*(C6), 12,899–12,918, doi:10.1029/97JC03415.

WAIS Divide Project Members (2013), Onset of deglacial warming in West Antarctica driven by local orbital forcing, *Nature*, doi:10.1038/nature12376.

Wyrtki, K. (1966), Oceanography of the Eastern Equatorial Pacific Ocean, in *Oceanography and Marine Biology*, vol. 4, edited by H. Barnes, pp. 33–68, George Allen & Unwin Ltd., London.

Wyrtki, K. (1967), Circulation and water masses in the eastern equatorial Pacific Ocean, *Int. J. Oceanol. Limnol.*, *1*(2), 117–147.

Wyrtki, K., and G. Meyers (1976), The Trade Wind Field Over the Pacific Ocean, *J. Appl. Meteorol.*, *15*(7), 698–704, doi:10.1175/1520-0450(1976)015<0698:ttwfot>2.0.co;2.